nuclear fusion
IAEA

PAPER • OPEN ACCESS

Isotope mass dependence of pedestal transport in JET H-mode plasmas

To cite this article: I. Predebon *et al* 2023 *Nucl. Fusion* **63** 036010

View the article online for updates and enhancements.

You may also like

- Isotope physics of heat and particle transport with tritium in JET-ILW type-I ELMy H-mode plasmas
P.A. Schneider, C. Angioni, F. Auriemma et al.
- The dependence of confinement on the isotope mass in the core and the edge of AUG and JET-ILW H-mode plasmas
P.A. Schneider, C. Angioni, L. Frassinetti et al.
- Isotope dependence of the type I ELMy H-mode pedestal in JET-ILW hydrogen and deuterium plasmas
L. Horvath, C.F. Maggi, A. Chankin et al.

This content was downloaded from IP address 117.86.172.57 on 21/10/2023 at 22:56

OPEN ACCESS
IOP Publishing | International Atomic Energy Agency
Nuclear Fusion
Nucl. Fusion **63** (2023) 036010 (12pp)
https://doi.org/10.1088/1741-4326/acb44f

Isotope mass dependence of pedestal transport in JET H-mode plasmas

I. Predebon[1,2], D.R. Hatch[3], L. Frassinetti[4], L. Horvath[5], S. Saarelma[5], B. Chapman-Oplopoiou[5], T. Görler[6], C.F. Maggi[5] and JET Contributors[a]

[1] Consorzio RFX (CNR, ENEA, INFN, Università di Padova, Acciaierie Venete SpA), Padova, I-35127, Italy
[2] Istituto per la Scienza e Tecnologia dei Plasmi, CNR, Padova, I-35127, Italy
[3] Institute for Fusion Studies, University of Texas at Austin, Austin, TX 78712, United States of America
[4] Division of Fusion Plasma Physics, KTH Royal Institute of Technology, SE-10691 Stockholm, Sweden
[5] CCFE, Culham Science Center, Abingdon OX14 3DB, United Kingdom of Great Britain and Northern Ireland
[6] Max Planck Institut für Plasmaphysik, D-85748 Garching, Germany

E-mail: italo.predebon@igi.cnr.it

Received 20 October 2022, revised 21 December 2022
Accepted for publication 18 January 2023
Published 2 February 2023



Abstract

We present a comparative transport analysis of the isotope mass dependence in the pedestal of two pairs of deuterium/hydrogen type I ELMy H-mode discharges in JET with ITER-like wall, one characterized by the same input power, the other one by the same stored energy. The investigation, carried out using the gyrokinetic code GENE, focuses on the steep profile region of the pedestal. While large wavenumber modes mainly contribute to the electron heat flux and are scarcely influenced by the main gas isotope, an effect of the ion mass in agreement with the experimental (so called anti-gyro-Bohm) scaling is revealed in the low wavenumber range. In this context, the major role played by the $E\times B$ shear in regulating the ion-temperature-gradient turbulence is analyzed in some detail. The competing level of turbulent and neoclassical transport is quantified to shed light on the experimental features of the pedestal profiles at different ion mass, with the particle transport found to be consistent with a higher pedestal top density for increasing isotope masses, and the heat transport shown to match the roughly unaltered observed temperature profiles.

Keywords: pedestal, isotope effect, transport, gyrokinetics, JET-ILW

(Some figures may appear in colour only in the online journal)

1. Introduction

The phenomenology of the pedestal represents one of the most interesting challenges for the magnetic fusion community. Despite the still incomplete comprehension of the physical processes leading to the formation and sustainment of the pedestal, for its high performance the H-mode is considered the principal mode of operation in most fusion devices. The reason for this partial lack of knowledge lies in the complexity of the system, with processes involving multiple spatial and temporal scales—from magnetohydrodynamics (MHD) to high-wavenumber turbulence—in the presence of large pressure gradients, further complicated by its role of junction between plasma core and separatrix region.

A decisive element pushing the tokamak community towards the adoption of the H-mode is the favorable scaling of the pedestal performance with the hydrogen isotope mass. As clearly shown in JET with ITER-like wall (ILW) [1, 2] and

[a] See Mailloux *et al* 2022 (https://doi.org/10.1088/1741-4326/ac47b4) for the JET Contributors.

Original Content from this work may be used under the terms of the Creative Commons Attribution 4.0 licence. Any further distribution of this work must maintain attribution to the author(s) and the title of the work, journal citation and DOI.

ASDEX Upgrade (AUG) [3], further confirmed in the recent JET DTE2 campaign, the height of the density pedestal progressively increases with the average mass of the hydrogen isotope, from protium (simply called hydrogen henceforth, H) to deuterium (D) to tritium (T), and from low to high concentration of T in a mixed DT plasma. Larger effective isotope masses are favorable to edge confinement. This improvement of confinement, not expected on the basis of the simplified gyro-Bohm scaling of transport, is commonly referred to as isotope effect, and presents important distinctions between plasma core and edge, and between density and temperature, as recently discussed in [4, 5].

Indeed, in JET-ILW and AUG the improvement of pedestal confinement is less evident in the temperature profiles. This is a rather strict constraint for any model attempting to describe the isotope effect in this region. Models pointing to peeling-ballooning (PB) stability as a candidate have revealed a small effect of diamagnetic stabilization at different ion masses [6]. On the other hand, the edge-localized mode (ELM) losses are seen not to change enough to account for major differences among isotopes. This is why inter-ELM transport is often claimed to be a potential player in this respect; in fact, this is the topic we are going to address for a restricted JET-ILW dataset.

The effect of the isotope mass in plasma turbulence may emerge on the basis of a different ρ_e/ρ_i (ratio of the electron to ion gyroradius), or a different ρ_* (ratio of the ion gyroradius to the plasma minor radius), or more likely both of them, possibly including an active role of the impurities. Depending on the dominant turbulence, one of the two parameters—ρ_e/ρ_i or ρ_*—may prevail. The former is especially important in trapped-electron-mode (TEM) turbulence: in [7] the anti-gB scaling of transport is explained in terms of collisional TEM stabilization by the isotope ions with an associated increase of the impact of zonal flows; in [8] the role of the non-adiabatic electron response is investigated to predict the DIII-D L-mode edge anti-gB scaling. On the other hand, typical JET-ILW pedestal profiles are more prone to ion-temperature-gradient (ITG) turbulence [9] (and electron-temperature-gradient (ETG) turbulence at high wavenumbers), where ρ_* is a crucial parameter and the interaction with macroscopic quantities like the $E\times B$ shear a decisive element [10, 11]. As a consequence, depending on the operational conditions adopted in the various tokamak devices (heating scheme, gas fuelling, impurities, etc), the action of the isotope mass on the pedestal transport is expected to differ.

In this paper, we consider the isotope effect in the pedestal of three JET-ILW discharges, two in D and one in H, designed to have one D–H pair with the same input power and the other one with the same stored energy. The plasma profiles of these *similar* pulses clearly show better performances of the D cases in terms of pedestal density, as shown in [1, 6]. In addition, we will artificially change the main ion mass (D to H, and vice versa) so as to disentangle pure isotope effects from profile effects, in an attempt to understand the possible inconsistencies introduced by a different ion mass. The latter has to be understood as a numerical experiment only, as any change of the main gas mass inherently implies modifications of the basic properties of the plasma through the scale ratios ρ_e/ρ_i and ρ_*, so that a pair of H/D experiments with the same (density *and* temperature) profiles and equilibria is never feasible [2]. Therefore the numerical investigation will be carried out for the three real (D, D, H) shots, plus three mass-modified (H, H, D) cases. The tool used for the analysis is GENE [12, 13], applied to realistic plasma equilibria and conditions for an investigation of neoclassical and electromagnetic turbulent transport. The aim of the paper is to identify the transport mechanisms affected and unaffected by changes of the main gas isotope.

The paper is organized as follows: after an introduction on the basic experimental properties of the selected dataset in section 2, and a description of the adopted numerical tools in section 3, we will deal with the neoclassical transport properties of the pedestal in section 4, and with the impact of turbulence on energy and particle transport at different spatial scales, from high wavenumbers (ρ_e-scale) in section 6, to low wavenumbers (ρ_i-scale) in section 7. A brief summary concludes the paper.

2. Experimental cases

We consider three JET-ILW pulses at $I_p = 1.4$ MA, $B_{\rm tor} = 1.7$ T, low triangularity, $\delta \sim 0.2$, and the same main gas rate, $\Gamma_e = 3-4\times 10^{21}$ e s^{-1}. Two pulses, #84793 and #84796, have D as the main ion species and one pulse, #91554, has H. These discharges have been selected to have a D–H pair characterized by the same stored energy (the pair #84793–91554) and a D–H pair characterized by the same input power (the pair #84796–91 554). The three pulses have only NBI heating, with $P_{\rm NBI} = 4.4$ MW for #84793 and $P_{\rm NBI} \approx 10$ MW for #84796 and #91554 (slightly higher for #84796). In the first D–H pair, the H pulse has approximately twice the heating power of the D pulse to reach the same stored energy; the resulting pedestal top pressure is similar, and the lower density in H is compensated by a higher temperature. In the second D–H pair, the comparable heating power results in similar temperatures, with the H pulse having a lower pedestal top pressure due to a reduced density.

The main engineering parameters of the experimental dataset are summarized in table 1. Apart from the main ion species and input power, the only difference is in the divertor configuration, with the D pulses having the inner strike point on the vertical target and the outer strike point on the horizontal target, while the H pulse is in the corner/corner configuration. The other macroscopic parameters are similar, the pulses being specifically selected from a larger database featuring the same plasma current, magnetic field and gas injection rate.

The three pulses have been thoroughly investigated from an experimental point of view in [1, 6, 14, 15]. The electron density and electron temperature profiles used in this work are the fits to the experimental pre-ELM (ELM: edge-localized mode) profiles determined using the method described in [16]. The fits to the pre-ELM experimental data are shown in figure 1; details on the profile mapping procedure will be reported in section 3. As anticipated, the density at the pedestal top is

Table 1. Main experimental parameters for the three JET-ILW pulses: #84793 (D), #84796 (D) and #91554 (H).

#	84 793	84 796	91 554
isotope	D	D	H
I_p (MA)	1.4	1.4	1.4
$B_{\rm tor}$ (T)	1.7	1.7	1.7
Γ_e (10^{21} e s^{-1})	3–4	3–4	3–4
δ	0.2	0.2	0.2
divertor config.	V/H	V/H	C/C
$P_{\rm NBI}$ (MW)	4.4	10.6	10.0
$W_{\rm tot}$ (MJ)	1.2	1.9	1.1

higher in both the D shots ($n_{e,\rm ped} \approx 3.0-3.5\times10^{19}$ m^{-3}) than in H ($n_{e,\rm ped} \approx 2\times10^{19}$ m^{-3}); the temperature at the pedestal top is comparable in the pair with the same input power ($T_{e,\rm ped} \approx 0.6$ keV) and is lower in the D pulse of the D–H pair with the same stored energy ($T_{e,\rm ped} \approx 0.4$ keV).

All the three pulses have type I ELMs, as shown by the increasing ELM frequency with power through the separatrix [1]. The ELM frequency is higher in the H pulse ($f_{\rm ELM} \approx 30$ Hz) than in the D pulses ($f_{\rm ELM} \approx 14$–19 Hz), while the ELM energy losses are comparable in the pair with the same stored energy ($\Delta W_{\rm ELM} \approx 75$ kJ) and are higher in D ($\Delta W_{\rm ELM} \approx 125$ kJ) in the pair with the same NBI power [6].

Concerning the pedestal stability, using the common JET assumption that $T_{e,\rm sep} = 100$ eV, the pre-ELM pedestal is limited by ideal PB stability in #84796 (i.e. the pre-ELM pedestal reaches the ideal PB stability boundary). The other D pulse is slightly further from the ideal PB stability limit (but rather close considering the error bars). Instead the H pulse does not seem to have the pedestal limited by ideal PB stability.

The inter-ELM transport and/or a different ELM transport are likely the key physical mechanism to explain the difference in the pedestal between H and D plasmas [6]. While a different neutral penetration does not seem to have a significant effect in determining the pedestal density in H and D plasmas, the ELM particle losses might play a role, although they might not fully explain the difference in the density. EDGE2D-EIRENE simulations performed for the D–H pair with the same stored energy suggest that the hydrogen pedestal might have slightly higher particle diffusivity transport coefficient in the pedestal region, while the heat diffusivity is roughly comparable [6].

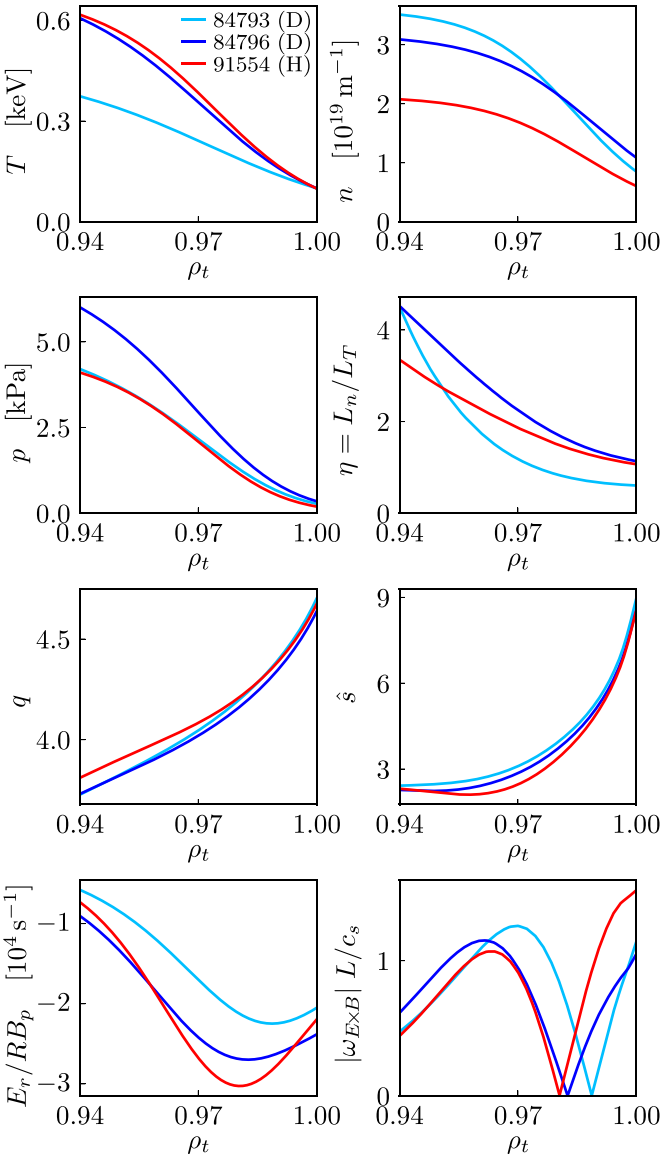


Figure 1. Main profiles and related quantities: temperature, density, total plasma pressure $p = p_i + p_e$, ratio of temperature to density logarithmic gradient η, safety factor, magnetic shear $\hat{s} = (\rho_t/q)(\mathrm{d}q/\mathrm{d}\rho_t)$, force-balance equation term $-\mathrm{d}\Phi_0/\mathrm{d}\Psi = E_r/RB_{\rm pol}$, and $E\times B$ sharing rate.

3. Numerical setup

The numerical simulations presented in this paper have been obtained using the gyrokinetic code GENE either in local or global mode [12, 13, 17]. Depending on the spatial scales of interest, we have exploited one or the other approach. Very briefly, we recall that in local simulations the spatial domain is a flux-tube assumed to be radially small compared to the system length scale, where the density, the temperature and the respective gradients are kept radially constant; periodic boundary conditions are applied, using spectral methods in the radial direction, and with an analytic expression of the gyroaverage operator. In global simulations the variation of the profiles and metric is allowed, adopting finite-difference schemes in the radial direction and suitable interpolations in the gyroaverage operator, as well as proper boundary conditions of the problem. In either case, the simulations have been performed with realistic parameters of the plasma, with some simplifying assumptions to make the numerical calculations more tractable.

An important limitation is indeed the split of the nonlinear analysis in high- and low-wavenumber turbulence, even though the assumption of scale separation is known to be questionable and potentially leading to wrong conclusions [18–20]. In most of the computations we consider two species—main

ions (D or H) and electrons—except for some nonlinear simulations in the ρ_e-scale range where an adiabatic ion response is assumed. Additional impurities are not included; they are partially taken into account by $Z_{\rm eff} \neq 1$. Parallel magnetic field fluctuations $B_\parallel$ are not included. Realistic values of β (the ratio of plasma to magnetic pressure) are adopted, while the collisions are modeled by means of a Landau-Boltzmann collision operator.

The gyrokinetic equation is solved in the 5-dimensional space $(x, y, z, v_\parallel, \mu)$ plus time, where x, y, and z are the radial, binormal, and parallel coordinates, respectively, $v_\parallel$ the parallel velocity and μ the magnetic moment. Specific details concerning the discretization and the grid size will be described after the definition of the single physical problem in the respective sections.

3.1. Magnetic equilibria and profile mapping

The magnetic equilibria have been built with the code HELENA [21]. To ensure the validity of our numerical results with respect to the bootstrap current model, we considered reconstructions using Hager's [22] and Sauter's [23] expressions for $j_{\rm BS}$. The density and temperature mapping on the flux surfaces practically coincides for the two models; only the safety factor and the magnetic shear are slightly different, but such that, based on a set of local linear gyrokinetic calculations, there are no substantial deviations in terms of growth rates and real frequencies. Thus while the choice of the bootstrap current model is generally relevant to determine the PB stability boundary [14], it turns out to be less important in a gyrokinetic framework (at least for the cases of this paper). With this caveat, we have adopted Hager's expression for our reconstructions.

Hereafter $\rho_t = (\psi_t/\psi_{t,\rm lcms})^{1/2}$ is used as a normalized radial coordinate, where ψ_t is the toroidal flux and $\psi_{t,\rm lcms}$ its value at the last closed magnetic surface. The magnetic equilibria are up-down asymmetric; in the steep profile region ($\rho_t \simeq 0.98$) the elongation of the flux surfaces is $\kappa \simeq 1.55$ for all the three discharges, while the up/down average triangularity is $\delta \simeq 0.22$ for #84793, $\delta \simeq 0.23$ for #84796, and $\delta \simeq 0.21$ for #91554, following the shape parameter definitions of [24].

Concerning profile mapping, for our dataset we assume the ion and electron temperature to be equal, $T_i = T_e$, due to the uncertainties in the ion temperature measurements. We remark that this choice can have an impact on the gyrokinetic simulation results. Let us define the normalized temperature and density gradients for the jth species as $1/L_{T_j} = -(\mathrm{d}T_j/\mathrm{d}\rho_t)/T_j$ and $1/L_{n_j} = -(\mathrm{d}n_j/\mathrm{d}\rho_t)/n_j$, respectively, and their ratio $\eta_j = L_{n_j}/L_{T_j}$. Having the same temperature profiles in a two-species plasma implies $\eta_i = \eta_e$. The stability of ITG (resp. ETG) modes is largely related to η_i (η_e). In principle an imbalance between η_i and η_e may result in the enhancement or suppression of ITG vs ETG turbulence, in the enhancement of TEM turbulence, or in the emergence of electromagnetic (e.g. microtearing) turbulence. Sensitivity analyses within the error bars of T_e and T_i are thus necessary to establish the robustness of the simulated transport levels, left to future studies due to computational resource constraints.

3.2. $E\times B$ shear

In the context of low-wavenumber turbulence a decisive role is played by the $E\times B$ shearing rate [25, 26], particularly in conditions with large pressure gradients such as the pedestal. Here the ion pressure gradient itself represents the dominant contribution to the radial electric field, as confirmed by accurate experimental studies in the plasma edge [27, 28]. Given the uncertainties in the measured flow, we assume a vanishing parallel mean flow given by the neoclassical expression $V_\parallel \propto \left(p_i'/n_i + Ze\,\Phi_0' - k_\parallel T_i' B^2/\langle B\rangle^2\right)$, where Φ_0 is the electrostatic potential, $k_\parallel$ is a dimensionless coefficient discussed e.g. in [29], and $\cdot' = \mathrm{d}\cdot/\mathrm{d}\psi$ denotes derivatives with respect to the poloidal magnetic flux ψ. We remark that, even if non dominant in H-mode pedestals, the inclusion of the toroidal flow is certainly to be considered for more accurate turbulent transport evaluations.

The $E\times B$ shearing rate is included in GENE in the form $\omega_{E\times B} = (\rho_t/q)\,\mathrm{d}(E_r/B_{\rm pol}R)/\mathrm{d}\rho_t$. As widely evidenced in the literature regarding the H-mode, the radial profile of $\omega_{E\times B}$ has large variations in the pedestal. For the three pulses presented here, it changes sign around $\rho_t \simeq 0.98$, indeed where the plasma profiles are steeper, see figure 1.

3.3. Pedestal profiles

The relevant radial profiles in the pedestal region of the three pulses are summarized in figure 1, where also the safety factor q and the magnetic shear are shown. The radial domain covered in the plots corresponds to a rather short spatial range in physical units. On the outboard midplane, the distance between the surface $\rho_t = 0.95$ and the last closed magnetic surface, $w_{\rm ped} = (R_{\rm lcms} - R_{\rho_t=0.95})|_{Z=0}$, is approximately 2.4 cm for pulse #84793, 2.2 cm for #84796, and 2.5 cm for #91554. The ratio of this distance to the ion gyroradius at mid-pedestal ($\rho_t = 0.97$) is $w_{\rm ped}/\rho_{\rm D} \simeq 18$ for pulse #84793, $w_{\rm ped}/\rho_{\rm D} \simeq 13$ for #84796, and $w_{\rm ped}/\rho_{\rm H} \simeq 20$ for #91554. In a radial interval of five ion gyroradii the density and temperature drastically change, e.g. with a jump $\Delta n_e \simeq 0.8\times 10^{19}$ m^{-3} and $\Delta T_e \simeq 200$ eV for pulse #84796. In contrast, in the region of the X-point such extreme gradients are relaxed, and the distance between the separatrix and the surface $\rho_t = 0.95$ almost reaches 20 cm.

3.4. Normalization and gB units

As mentioned in the introduction, each of the three experimental cases will be investigated by additionally changing the mass of the main gas: $m_{\rm D} \to m_{\rm H}$ for #84793 and #84796, $m_{\rm H} \to m_{\rm D}$ for #91554. In this procedure the ion gyroradius ρ_i and the ion sound speed $c_i = (T_e/m_i)^{1/2}$ are inherently modified. Taken H as the fundamental species and defined the mass ratio $A_i = m_i/m_{\rm H}$, for an arbitrary gas species with mass m_i and charge Z_i the gyroradius and the ion sound speed scale as $\rho_i/\rho_{\rm H} = A_i^{1/2}/Z_i$ and $c_i/c_{\rm H} = A_i^{-1/2}$.

Normalized species units are commonly used in the gyrokinetic formalism. For a generic scalar quantity σ in physical units, we will use the notation $\widetilde{\sigma}_{(i)}$, with $i =$ H or D, for

its normalization in H or D species units, respectively. For instance, rates and frequencies are usually expressed as $\widetilde{\gamma}_{(i)} = \gamma L/c_i$ (with L the system length scale), spatial scales and wavenumbers as $\widetilde{\xi}_{(i)} = \xi/\rho_i$ and $\widetilde{k}_{(i)} = k\rho_i$, respectively, and fluxes as $\widetilde{\Gamma}_{(i)} = \Gamma/\Gamma_{\mathrm{gB},i}$ and $\widetilde{Q}_{(i)} = Q/Q_{\mathrm{gB},i}$, where $\Gamma_{\mathrm{gB},i} = n_i c_i \rho_{*i}^2$ and $Q_{\mathrm{gB},i} = p_i c_i \rho_{*i}^2$ are the gyro-Bohm (gB) particle and heat fluxes, respectively, with $\rho_{*i} = \rho_i/L$.

More specifically, a change of the isotope mass $m_\mathrm{D} \leftrightarrow m_\mathrm{H}$ introduces factors of $A_\mathrm{D}^{1/2}$ in the normalized rates and frequencies in species units, $\widetilde{\gamma}_{(\mathrm{D})} = A_\mathrm{D}^{1/2}\widetilde{\gamma}_{(\mathrm{H})}$, for any quantity γ measured in s^{-1}. As an example, the ν_{ei} collision frequency depends on the electron mass only, and the $\omega_{E\times B}$ shearing rate depends on macroscopic quantities independent of the isotope mass, therefore they do not change in physical units (measured in s^{-1}), consequently $\widetilde{\nu}_{ei\,(\mathrm{D})} = A_\mathrm{D}^{1/2}\widetilde{\nu}_{ei\,(\mathrm{H})}$ and $\widetilde{\omega}_{E\times B\,(\mathrm{D})} = A_\mathrm{D}^{1/2}\widetilde{\omega}_{E\times B\,(\mathrm{H})}$. On the other hand, the ν_{ii} collision frequency depends on $m_i^{-1/2}$, thus $\widetilde{\nu}_{ii\,(\mathrm{D})} = \widetilde{\nu}_{ii\,(\mathrm{H})}$.

Normalized spatial scales change with opposite trend in species units: $\widetilde{\xi}_{(\mathrm{D})} = A_\mathrm{D}^{-1/2}\widetilde{\xi}_{(\mathrm{H})}$ for any length ξ (measured in m), and $\widetilde{k}_{(\mathrm{D})} = A_\mathrm{D}^{1/2}\widetilde{k}_{(\mathrm{H})}$ for the wavenumbers (measured in m^{-1}). Incidentally, a consequence is that for a given pedestal width w_ped the flux-tube approximation is more reliable in H than in D, since $\widetilde{w}_{\mathrm{ped\,(H)}} > \widetilde{w}_{\mathrm{ped\,(D)}}$. Global simulations covering the whole pedestal necessarily have a different discretization in species units in the radial direction: for the same number of radial grid points n_x, the mesh spacing in species units is $\widetilde{\Delta x}_{(\mathrm{D})} = A_\mathrm{D}^{-1/2}\widetilde{\Delta x}_{(\mathrm{H})}$ (the grid is more dense in D than in H), and on the other hand to keep the same $\widetilde{\Delta x}_{(i)}$, the number of grid points is $n_{x_\mathrm{D}} = A_\mathrm{D}^{-1/2} n_{x_\mathrm{H}}$ (less requirements in D than in H). We will use the latter approach, whenever possible.

Based on the H fluxes, we have $\Gamma_{\mathrm{gB},i}/\Gamma_{\mathrm{gB,H}} = Q_{\mathrm{gB},i}/Q_{\mathrm{gB,H}} = A_i^{1/2}/Z_i^2$. In particular, for a change $m_\mathrm{D} \leftrightarrow m_\mathrm{H}$, $\Gamma_{\mathrm{gB,D}}/\Gamma_{\mathrm{gB,H}} = Q_{\mathrm{gB,D}}/Q_{\mathrm{gB,H}} = A_\mathrm{D}^{1/2}$. In the unfortunate case of gB-scaling of the energy flux, one obtains an unfavorable transport increase with the isotope mass as $A_\mathrm{D}^{1/2}$. This is expected, e.g. for the ion heat flux in local ITG turbulence with an adiabatic electron response or in local neoclassical transport evaluations. As mentioned in the introduction, elements coupling the ion and the electron dynamics (like the electron-ion collisionality or the electron-to-ion mass ratio) or the ion-scale with the system scale (like ρ_{*i} or the shear flow) break the H/D isomorphism. In order to compare measurable H vs D performance, we will often write the fluxes Γ and Q in physical units.

4. Neoclassical transport

Neoclassical transport is usually relevant in the pedestal, at least in the ion heat channel. The plasma in this region is usually in a banana/plateau collisional regime. In general, the ion heat diffusivity χ_i is expected to exceed the electron heat diffusivity χ_e by a factor $\sim (m_i/m_e)^{1/2}$, with χ_e being comparable to the ambipolar particle diffusivity D [30]. In many experimental scenarios χ_i turns out to fit the data satisfactorily, see, e.g. [31, 32].

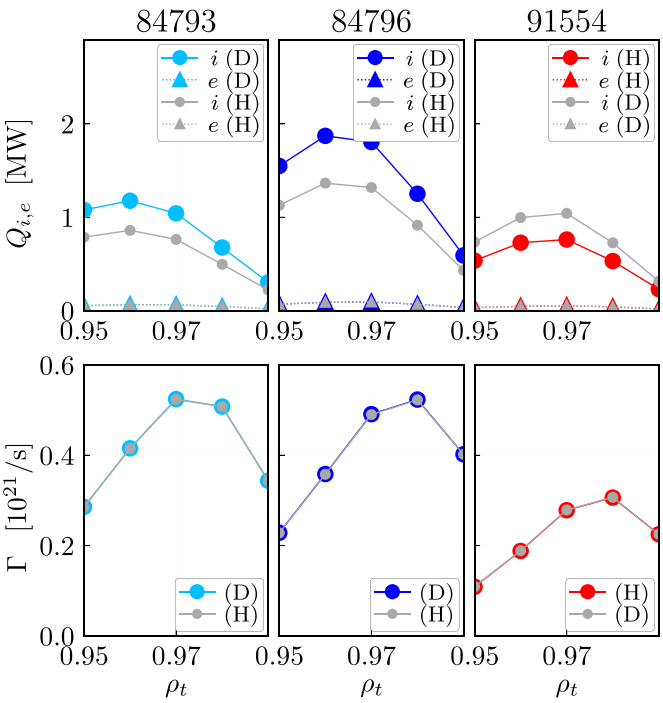


Figure 2. Neoclassical ion (circles) and electron (triangles) heat fluxes (upper frames) and particle fluxes (lower frames) integrated over the flux surfaces, calculated with GENE. The colored symbols correspond to the nominal main gas isotope (D, D, H), the gray ones to the switched isotopes (H, H, D, respectively).

We address the role of neoclassical particle and heat transport using the code GENE, which is used here as a neoclassical equilibrium solver in the flux-tube limit; in this approximation, the neoclassical equation is contained in the gyrokinetic equation as its perturbed, non-fluctuating part, being therefore decoupled from turbulence. Considering only the component $(k_y, k_x) = (0,0)$, for the present analysis we set a discretization in the velocity space $(n_{v_\parallel}, n_\mu) = (96, 64)$, with $n_z = 192$ points in the longitudinal direction. The fluxes are then computed as velocity space moments of the non-fluctuating part of the perturbed distribution function. A comparison with the code NEO [33, 34] for the three pedestals (carried out only for the nominal main gas isotope) proved to be satisfactory.

The neoclassical heat and particle fluxes are shown in figure 2 for the radial domain $\rho_t \in [0.95, 0.99]$. The high-pressure D case #84796 exhibits the largest ion heat flux across the pedestal. The low-density H shot #91554 has a neoclassical particle flux which is approximately halved with respect to the other cases. We notice in figure 3 that, in gB units, the normalized $\widetilde{Q}_{(i)}$ and $\widetilde{\Gamma}_{(i)}$ fluxes have similar radially increasing trends, being larger for the D pulse #84793 in a large part of the pedestal and converging towards comparable values in the outer radial domain. Thus the profiles of the fluxes in physical

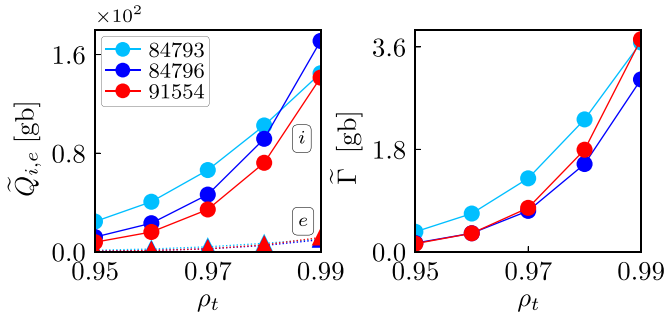


Figure 3. Neoclassical ion and electron heat fluxes (left frame) and particle fluxes (right frame) in gyro-Bohm units for the nominal main gas isotope.

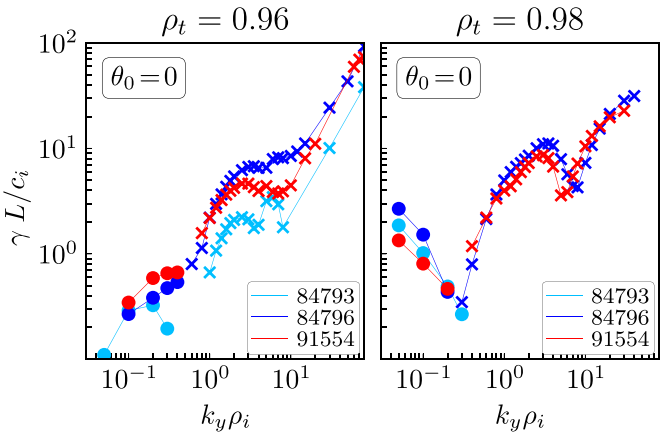


Figure 4. Normalized growth rate in species units (c_i is the ion sound speed, L the characteristic length of the system) as a function of the normalized wavenumber $k_y\rho_i$ for $\theta_0 = 0$, at $\rho_t = 0.96$ (left) and $\rho_t = 0.98$ (right) from local linear simulations. Dots (resp. crosses) represent modes with positive (negative) real frequency, i.e. propagating in the ion (electron) diamagnetic direction.

units largely come through the dependence of $Q_{\mathrm{gB},i}$ and $\Gamma_{\mathrm{gB},i}$ on p_i and n_i, respectively.

The artificial switch of the isotope mass $m_\mathrm{D} \leftrightarrow m_\mathrm{H}$ does not influence the electron heat flux Q_e nor the ambipolar particle flux Γ. On the other hand, independently of the collisional regime, the ion heat flux is expected to scale as $Q_{i\,(\mathrm{D})}/Q_{i\,(\mathrm{H})} \sim (m_\mathrm{H}/m_\mathrm{D})^{1/2}(\rho_\mathrm{D}/\rho_\mathrm{H})^2 = A_\mathrm{D}^{1/2}$, where the factor $(m_\mathrm{H}/m_\mathrm{D})^{1/2}$ comes either from $\nu_\mathrm{D}/\nu_\mathrm{H}$ in the banana regime (where $\nu_i \propto m_i^{-1/2} Z_i^4 n_i / T_i^{3/2}$) or from $c_\mathrm{D}/c_\mathrm{H}$ in the plateau regime.

The gB-scaling of the ion heat transport is in fact almost satisfied in the realistic conditions of our three pedestals. More precisely, the ratio $\widetilde{Q}_{i\,(\mathrm{D})}/\widetilde{Q}_{i\,(\mathrm{H})}$ in gB units is between 0.96–0.97 at all radii. This reflects in a dependence $Q_{i\,(\mathrm{D})}/Q_{i\,(\mathrm{H})} = A_\mathrm{D}^\alpha$ with $\alpha \in [0.44, 0.46]$ in physical units. Having similar normalized heat flux profiles and practically overlapping pressure profiles, the pulses #84793 and #91554 turn out to have comparable neoclassical ion heat fluxes when the same isotope is imposed.

These results have been obtained in a local approximation. As pointed out in [35], and more specifically in [36] for a study on the isotope effect, in the case of steep plasma profiles and for the larger isotope masses the local approximation provides inaccurate results. In particular, the expected gB dependence of the ion heat flux is mitigated in a radially global context and bringing to a favorable isotope scaling trend [36], though far from being an anti-gB scaling. With this caveat, we have nonetheless used the local approach for the sake of simplicity.

5. Instabilities in the pedestal

A large variety of instabilities usually occurs in the region of the pedestal due to the large density and temperature gradients, and, as a direct consequence, due to a different ordering of the diamagnetic frequency ω_* with respect to the plasma core. With ω_* greatly exceeding the magnetic drift frequency ω_d, slab resonances may easily occur, providing a weak (or even opposite) dependence of the growth rates on the ballooning angle θ_0 with respect to the plasma core [9], where, in contrast, the modes are mainly driven by toroidal resonances with the curvature and ∇B drifts. This feature of the pedestal, together with the concurrent high shaping of the flux surfaces, causes the emergence of peculiar geometric features of the modes, often peaked off the outboard midplane, most commonly close to top/bottom of the flux surfaces. Some of these features disappear in a nonlinear context, others are retained.

In order to provide an overview of the instabilities at play, first we consider the local approximation as a starting point for the following more in-depth analysis. Only the nominal isotope is considered in this section. In the top of the pedestal, for $\rho_t \lesssim 0.95$, microtearing modes are found to be slightly unstable ($\gamma \ll 1$) for $k_y\rho_i \ll 1$, while for larger wavenumbers ITG and ETG modes are dominant for $k_y\rho_i \lesssim 1$ and $k_y\rho_i \gtrsim 1$, respectively. Moving from the pedestal top towards the steep profile region and the separatrix, the ITG wavenumber range gradually reduces its extent, kinetic-ballooning-modes (KBMs) are progressively enhanced at low wavenumbers while the ETG range enlarges with the appearance of two distinct branches. In figure 4 we show the results for two radii, for simplicity at $\theta_0 = 0$ only, such that they can be considered only partially representative of the whole set of unstable modes. At $\rho_t = 0.96$ (slightly down the pedestal top), for all the three pulses the modes at $k_y\rho_i < 1$ with positive real frequency ω (i.e. propagating in the ion diamagnetic direction) are ITG modes; for larger wavenumbers, the most unstable modes are ETG modes, with the peak occurring for $1 \lesssim k_y\rho_i \lesssim 10$ corresponding to the toroidal-ETG branch, and the branch for higher wavenumbers to slab-ETG [37]. At $\rho_t = 0.98$ (steep pedestal region), KBMs dominate at low $k_y\rho_i$, while for the ETG modes the distinction between toroidal and slab branches is evident.

Particular care is needed when dealing with KBMs in the pedestal, as their radial extent can easily exceed the pedestal width, making their description incompatible with the results of local gyrokinetic simulations. In [9], a criterion is identified to establish whether or not a strongly ballooning mode (such as the KBM) within the local approximation has a radial structure consistent with the narrow radial width of the pedestal,

and ultimately whether or not the mode can be considered physical. Based on this criterion, local KBMs have been identified as unphysical, at least for the pedestals described in [9]. A global approach is therefore needed. We disclose now that the KBMs present at low wavenumbers in figure 4 indeed disappear in global simulations. As noted in [9] however, the use of more realistic boundary conditions including a vacuum solution beyond the separatrix may have an impact on global results, possibly leading to different conclusions regarding the KBM turbulence contribution to the total pedestal transport.

More details and more quantitative evaluations are in the next two sections, where we will consider two limits: (a) a local approach for ρ_e-scale instabilities and turbulence, which takes advantage of the flux-tube approximation; (b) a global approach for ρ_i-scale instabilities and turbulence, which takes into account profile variations. While we are aware of the intrinsic conceptual difficulties underlying scale-separation—also proved by results showing the tendency of large-scale turbulence to suppress small-scale turbulence, and of the small-scale turbulence to weaken large-scale structures [20]—we insist on keeping this approach to make the study numerically feasible. The isotope effect will be discussed for each limit separately.

6. ρ_e-scale stability and transport

ETG turbulence is expected to yield a substantial fraction of the total heat transport in the pedestal [38], thus it needs to be quantified together with the other active transport processes for an overall evaluation of the heat losses. On the other hand, ETG turbulence is not expected to be an effective mechanism underlying the isotope effect, as it causes almost exclusively electron heat transport largely decoupled from the ion dynamics, and low particle flux. Indeed, in this section we will mainly investigate the latter problem rather then focusing on the fraction of heat transport supplied by ETG turbulence compared with the other transport sources.

6.1. Stability

Both toroidal and slab ETG modes are usually present in the steep profile region of the pedestal. We do not report here the details on the mode structure in the (k_x, k_y) space; a comprehensive analysis on this topic is reported, e.g. in [37–39] and [40]. In this region, the modes usually peak off-midplane in θ_0, with two or three asymmetric peaks.

For the purpose of the paper, let us deal again with the $\theta_0 = 0$ section, and consider the effect of a change of the isotope on linear stability for a two-species plasma. In figure 5, only the modes with negative real frequency (here, ETG) are shown for shot #84796. For clarity, all the quantities are rescaled to electron units, showing $\gamma L/c_e$ as a function of $k_y\rho_e$. As a consequence of the change of mass $m_\mathrm{D} \to m_\mathrm{H}$, the growth rates result practically unchanged, both for the high-k_y slab branch and for the low-k_y toroidal branch. The same behavior holds true for $\theta_0 \neq 0$.

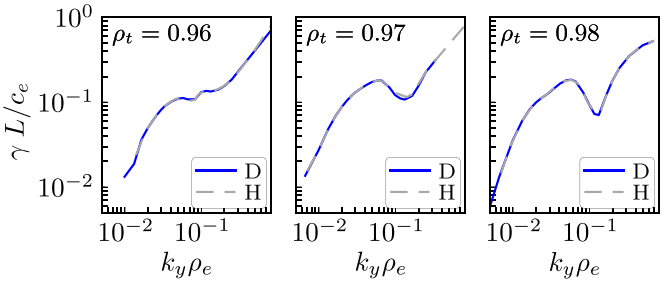


Figure 5. Normalized growth rates in electron units, where $c_e = (T_e/m_e)^{1/2}$, for pulse #84796 at 3 radii, with $\theta_0 = 0$ and kinetic ion response from local linear simulations. Solid blue lines represent the nominal isotope (D), dashed gray lines the changed isotope (H).

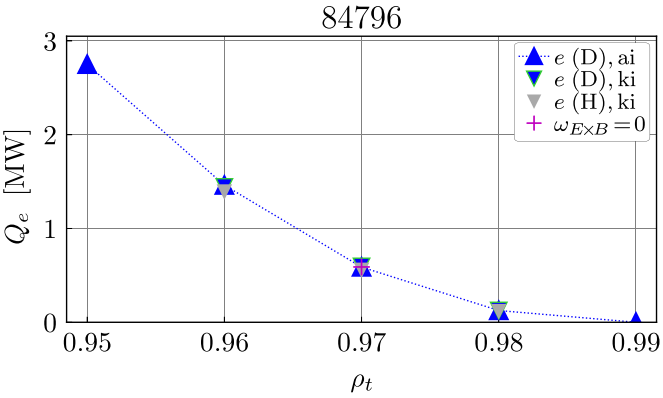


Figure 6. ρ_e-scale electron heat flux integrated over the flux surfaces for #84796, calculated with GENE in local approximation with adiabatic ion response (e (D), ai), with kinetic ion response (e (D), ki), and with kinetic ion response and switched isotope (e (H), ki). For $\rho_t = 0.97$ also the case with $\omega_{E\times B} = 0$ in D is shown.

Based on this simplified study, we expect ETG turbulence alone not to be responsible for the isotope effect, at least for the wavenumber range explored here.

6.2. Transport

We have performed a set of nonlinear simulations to resolve the corresponding high wavenumber turbulence for pulse #84796. Both an adiabatic and a kinetic ion response are assumed for this purpose.

For the grid discretization in the (k_y, k_x) sub-space, we set a box with 128×256 elements with $\Delta k_y \simeq 2$–3 and $\Delta k_x \simeq 2$, depending on the radius. In the velocity subspace we set $n_{v_\parallel} = 32$, $n_\mu = 8$: convergence tests with $n_{v_\parallel} \times n_\mu$ up to 64×16 have shown that the such values yield reliable saturated transport levels, i.e. not under/over-estimated with respect to cases with higher resolution. Along z we set $n_z = 192$; again, tests with higher n_z show that the fine structures developing in the longitudinal direction are sufficiently resolved.

In figure 6 we show the resulting electron heat flux as a function of ρ_t. For this pulse the contribution of ETG turbulence to the heat transport turns out to be important especially in the top of the pedestal, then decreasing towards the edge. The heat fluxes have been computed (a) with an adiabatic ion

response in the full radial domain, (b) with kinetic (nominal) D ions, and (c) with kinetic (switched) H ions in the subdomain $\rho_t \in [0.96, 0.98]$. For the comparison D/H, an equal wavenumber discretization has been set in ρ_e units while changing the mass, i.e. $\Delta k_{x,y}\rho_{\rm H} = A_{\rm D}^{-1/2}\Delta k_{x,y}\rho_{\rm D}$. As is evident, the heat fluxes are practically overlapped, with a negligible impact of the isotope mass, thus confirming the expectations from the linear analysis. In addition, for a single radial position and with kinetic D ions, setting $\omega_{E\times B} = 0$ does not influence appreciably the saturated transport level, as expected in high wavenumber turbulence. Furthermore, in the presence of kinetic ions, the ion heat flux Q_i represent a small fraction of Q_e (between 1/40 and 1/20), and the particle flux is almost negligible compared to the neoclassical flux, with the ratio $\Gamma_{\rm ETG}/\Gamma_{\rm NEO}$ ranging from 1/10 to 1/100, decreasing from the pedestal top to the edge, and being scarcely affected by the main gas isotope mass.

Summarizing this section, neither a finite shearing rate nor the change of the main ion mass produce remarkable differences with respect to the nominal case, at least in our large Δk_y and Δk_x nonlinear simulations. For this reason ETG turbulence, albeit important in terms of total heat flux released across the pedestal (cf Q_e from ETG turbulence in figure 6 vs Q_i from neoclassical transport in figure 2), will not be further considered in the context of the paper, where we will instead focus only on the mechanisms known to be affected by the isotope mass.

7. ρ_i-scale stability and transport

With ρ_i-scale we refer to the wavenumber range $k_y\rho_i \lesssim 1$. As mentioned previously, the large profile variations present in a pedestal make the local approximation questionable for modes with a large—comparable with the pedestal width—radial extent. This is true not only for the KBMs, but also for the ITG radial envelope in nonlinear simulations.

7.1. Stability

Before moving to global simulations, let us consider once more the dependence of the linear stability on the isotope mass at low wavenumbers in a flux-tube domain. In figure 7, the growth rates are shown in species units for $k_y\rho_i \leqslant 0.5$ with the nominal main gas (upper panels), and after the switch of the isotope mass (lower panels). With respect to figure 4, here we take the maximum growth rate over θ_0 for each wavenumber k_y. Comparing the top and bottom panels we note that: (a) the modes with $\omega < 0$ appearing at the largest wavenumbers are ETG modes, whose wavenumbers and growth rates change according to $\widetilde{k}_{y\,({\rm H})} = A_{\rm D}^{-1/2}\widetilde{k}_{y\,({\rm D})}$ and $\widetilde{\gamma}_{({\rm H})} \simeq A_{\rm D}^{-1/2}\widetilde{\gamma}_{({\rm D})}$, having approximately the same values of $\gamma(k_y)$ in physical or electron units; in species units (figure 7) they result in a leftward & downward (resp. rightward & upward) shift of the points for a change of mass $m_{\rm D} \to m_{\rm H}$ ($m_{\rm H} \to m_{\rm D}$); (b) the dependence of KBM and ITG growth rates on the isotope mass is rather weak and somewhat unclear. Only for $\rho_t = 0.96$,

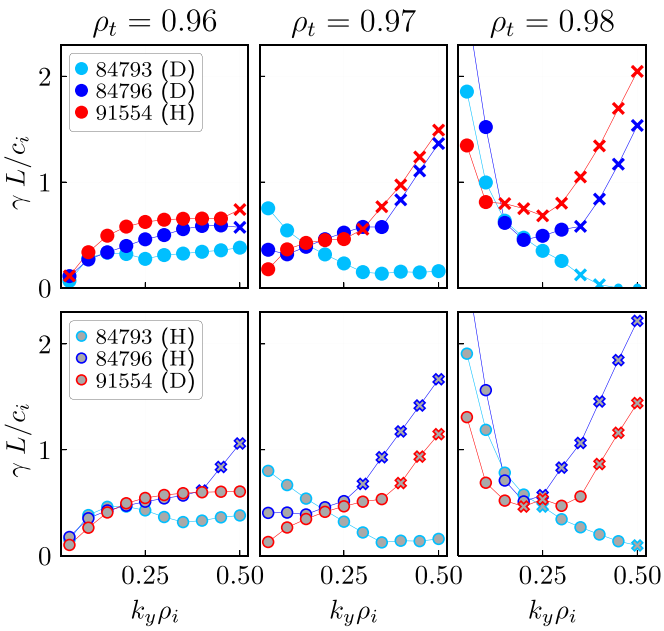


Figure 7. Normalized growth rates (maximum over θ_0) in species units from local linear calculations for the nominal isotope (upper panels) and for the switched isotope (lower panels). Circles (crosses) represent modes with positive (negative) real frequency.

the linear simulations provide $\widetilde{\gamma}_{({\rm H})} \gtrsim \widetilde{\gamma}_{({\rm D})}$ at low wavenumbers, which is not sufficient to provide an anti-gB scaling of the transport, however. Furthermore, the evaluation of the transport coefficients ratios D/χ_i and χ_e/χ_i for each couple (k_y, θ_0), based on the analysis of transport fingerprints of pedestal modes [41], has not revealed a clear dependence on the isotope mass.

As mentioned previously, the KBMs dominating the range $k_y\rho_i \ll 1$ of local simulations could be unphysical, thus their presence must be confirmed in global simulations. With this aim, for the three pedestals we set a radial domain $\rho_t \in [0.945, 0.995]$ with a discretization of $n_x = 384$–512 grid points, and $n_z = 96$–128 grid points in the longitudinal direction. In the parallel velocity and magnetic moment space, the domain $(v_\parallel, \mu) \in [-4v_{\rm th}, 4v_{\rm th}] \times [0, 11\,T/B]$ is resolved with 64×24 grid points. Dirichlet boundary conditions are imposed in the radial direction; in order to damp the fluctuations in the proximity of the boundaries, a Krook operator is defined in a thin buffer zone added both to the inner and the outer bound of the radial domain. Convergence tests have been performed to set a reliable buffer size, amplitude and polynomial order of the operator. With respect to the local simulations, a finite hyperdiffusion coefficient needs also to be specified for a dissipation in the radial direction. As we did previously, two particle species are considered. Parallel vector potential fluctuations are retained, with experimental values of β. The $E\times B$ shear is not included here, as we prefer to separately investigate its role in the nonlinear context.

In figure 8 the growth rates are shown in species units as a function of the wavenumber $k_y\rho_i$. KBMs are no longer the most unstable modes; they could be subdominant, however; they could also be more unstable with more realistic boundary

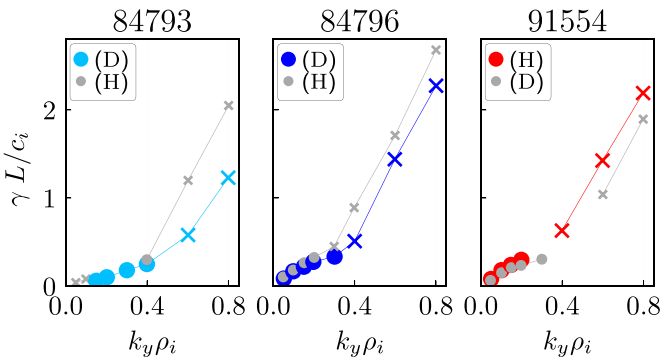


Figure 8. Normalized growth rates in species units from global linear simulations in the radial domain $\rho_t \in [0.945, 0.995]$ for the three pulses with nominal and switched isotope. Circles (crosses) represent modes with positive (negative) real frequency.

conditions, as commented previously. The instabilities with $\omega > 0$ are identified as ITG modes, those with $\omega < 0$ again as ETG modes. Starting from the latter, the increase (resp. decrease) of the growth rate for $m_D \to m_H$ ($m_H \to m_D$) is in line with the previous local calculations, resulting in overlapping $\gamma(k_y)$ curves when plotted in physical or electron units. On the other hand, a slight increase (resp. decrease) of the growth rates occurs in the ITG range. As for the local case, an assessment on the related transport can be attempted by estimating the relative weight of the heat fluxes and particle/heat fluxes driven by the single modes. In the ETG range, the ratios $Q_i/Q_e \ll 1$ and $\Gamma/Q_e \ll 1$ are almost unaffected by the isotope mass. In the ITG range, only for the pulse #84796 the ratio Γ/Q_i is lower in H than in D, meaning a higher ion heat flux with respect to the particle flux when $m_D \to m_H$; conversely, for the other two pulses this ratio does not change distinctively with the isotope mass. Therefore, at least for the present dataset, a clear isotope effect is not evident based on linear results.

To understand in more detail the mode structure in a global radial domain, we show in figure 9 the pattern of the electrostatic potential ϕ and of the parallel vector potential $A_\parallel$ fluctuations of the most unstable mode at two different wavenumbers in the (x, z) plane, averaged over k_y. The pulse #84796 with the nominal isotope (D) is considered here, but similar considerations are valid for the other cases. The low-wavenumber case is an ITG mode, with ϕ peaked in the vicinity of the X-point of the separatrix, and an antisymmetric pattern of $A_\parallel$. The high-wavenumber case is an ETG mode, with ϕ fluctuations more elongated in the z direction but again prominent close to the X-point, and with a fine structure in the radial direction.

7.2. Transport

For the nonlinear global simulations the basic setup is similar to the linear ones; in addition, adequate particle/heat sources are required, as well as the $E \times B$ shear as defined in section 3.2. For the radial mesh we set $n_x = 384$–512 to appropriately resolve the turbulent structures. Quasi-stationary simulations are obtained by including proper particle and heat sources,

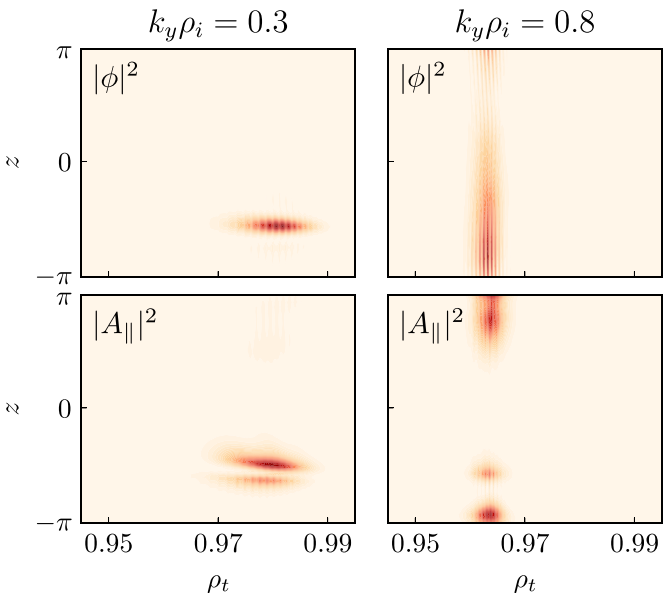


Figure 9. Fluctuation patterns of $|\phi(\rho_t, z)|^2$ (upper frames) and $|A_\parallel(\rho_t, z)|^2$ (lower frames) of the most unstable mode at $k_y\rho_i = 0.3$ (left) and $k_y\rho_i = 0.8$ (right) from global linear simulations for pulse #84796 with the nominal isotope (D).

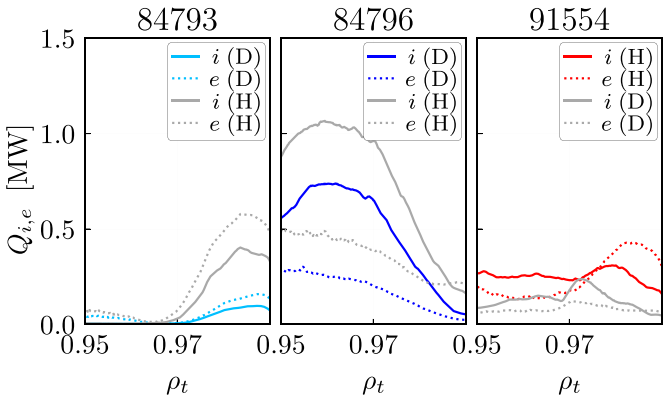


Figure 10. Ion and electron heat fluxes integrated over the flux surfaces for the nominal (colored lines) and switched (gray lines) isotope from global nonlinear GENE simulations.

which are modeled by means of a radially-distributed Krook-type particle/heat term on the right hand side of the Vlasov equation [13].

The results of the nonlinear analysis are in figure 10. Here we show the radial profiles of the ion and electron heat fluxes integrated over the flux surfaces, in physical units (MW). Interestingly, the swap of the isotope introduces an anti-gB scaling of the heat transport, with $Q_{(H)} \gtrsim A_D^{1/2} Q_{(D)}$. In gB units this reads $\widetilde{Q}_{i\,(H)} \gtrsim A_D \widetilde{Q}_{i\,(D)}$ for the ion heat flux, but the same is valid for the electron heat channel. For pulse #84796 the ion flux is roughly twice the electron one, while for the other pulses the ion and electron heat fluxes are comparable.

Clear differences exist in the radial profiles of the heat fluxes: for the high-pressure D case #84796, the largest values are in the upper part of the pedestal; for the low-temperature D case #84793, the profiles are larger in the outer part of the

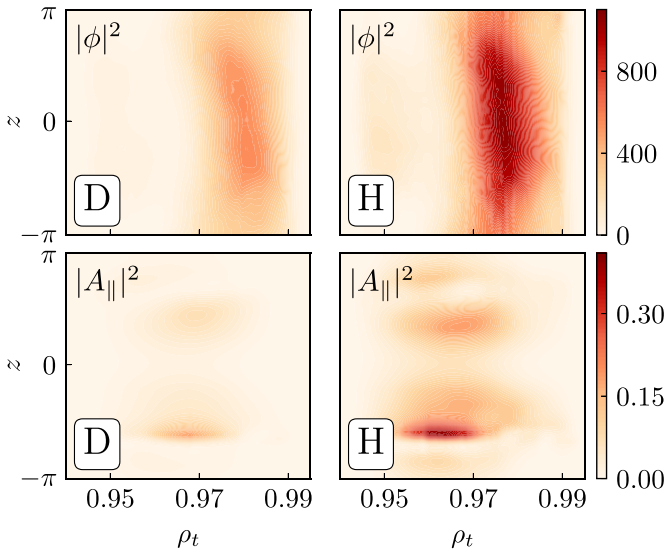


Figure 11. Fluctuation patterns of $|\phi(\rho_t,z)|^2$ (in units $\rho^* T_e/e$) and $|A_\parallel(\rho_t,z)|^2$ (in units $B\rho^*\rho_i$), averaged over k_y from global nonlinear simulations of pulse #84796, for the nominal isotope (left frames) and the switched isotope (right frames).

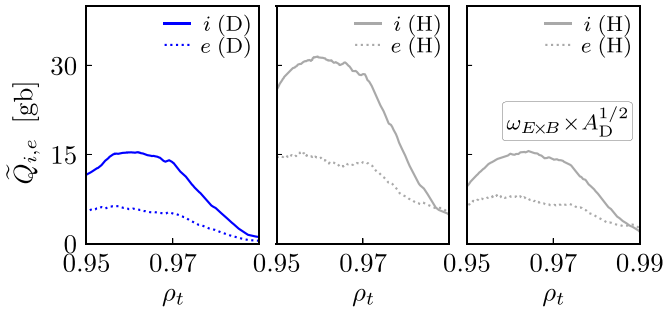


Figure 12. Ion and electron heat fluxes in gyro-Bohm units for the nominal isotope (left), the switched isotope (middle), and the switched isotope with $\omega_{E\times B}$ increased by $A_D^{1/2}$ (right), pulse #84796.

domain; for the low-density H case #91554, the profiles are rather uniform radially. Further investigation is needed to clarify such differences.

The pattern of the ϕ and $A_\parallel$ fluctuations in the (x,z) plane is shown in figure 11 for pulse #84796 for both D and H. In general, the fluctuation amplitude is larger in H than in D, and for the electrostatic potential is larger in the right hand side of the radial domain, i.e. in correspondence of the highest gradients of the pedestal. For our dataset, a comparison of the simulated fluctuation level with the experimental counterpart is not possible due to unavailability of the corresponding measurements. In this respect, however, it is interesting to recall that in AUG H-mode plasmas the pedestal density fluctuations measured by Doppler reflectometry have been found to be larger in H than in D [3].

As already pointed out, the swap of the isotope mass corresponds to a change of the normalized $\omega_{E\times B}$ rate in normalized species units for fixed pedestal profiles. Moving from D to H implies a decreased normalized $E\times B$ rate by a factor $2^{1/2}$, $\widetilde{\omega}_{E\times B\,(\mathrm{H})} = A_\mathrm{D}^{-1/2}\widetilde{\omega}_{E\times B\,(\mathrm{D})}$, with a consequent increase of the turbulent transport level; conversely, moving from H to D implies an increased normalized $E\times B$ rate by a factor $2^{1/2}$, $\widetilde{\omega}_{E\times B\,(\mathrm{D})} = A_\mathrm{D}^{1/2}\widetilde{\omega}_{E\times B\,(\mathrm{H})}$, with a consequent decrease of the turbulent transport level.

In general, in pedestals dominated by ITG turbulence and for fixed plasma profiles, heavier isotope masses ($m_\mathrm{T} > m_\mathrm{D} > m_\mathrm{H}$) are expected to cause lower turbulent heat fluxes ($Q_\mathrm{T} < Q_\mathrm{D} < Q_\mathrm{H}$).

As a verification of the role of the $E\times B$ shear, let us force for the case with the switched isotope the same normalized $\widetilde{\omega}_{E\times B\,(i)}$ as for the nominal isotope. If $m_\mathrm{D}\to m_\mathrm{H}$, this means an H plasma with $\widetilde{\omega}_{E\times B\,(\mathrm{H})}$ increased by a factor of $A_\mathrm{D}^{1/2}$, such that $\widetilde{\omega}_{E\times B\,(\mathrm{H})} = \widetilde{\omega}_{E\times B\,(\mathrm{D})}$. In figure 12, the $Q_{i,e}$ profiles are shown (now in gB units) for the nominal isotope (D for pulse #84796), the switched isotope (H), and the switched isotope with $\omega_{E\times B}$ increased by $A_\mathrm{D}^{1/2}$. The latter exhibits a Q_i profile rather similar to the case with the nominal isotope, confirming the role of $\omega_{E\times B}$ to establish the saturated transport levels. The electron heat flux Q_e follows the same behavior as Q_i, albeit less affected by the increased shearing rate.

The decrease of the ion heat transport with the isotope mass is in line with the scaling $\widetilde{Q}_{(i)} \propto \rho_{*i}^{-2} \propto \widetilde{\omega}_{E\times B\,(i)}^{-2}$ discussed in [11] for ITG turbulence, obtained both with adiabatic electrons and with the inclusion of kinetic electrons and electromagnetic effects. Since ITG turbulence is prevailing in our pedestals at low wavenumbers, the decorrelation theory described in [42, 43] is expected to fit the results, and the suggested scaling reads, in physical units,

$$Q_{(\mathrm{D})}/Q_{(\mathrm{H})} \sim A_\mathrm{D}^{-1/2} \qquad \text{ITG turbulence.}$$

We note that this scaling is valid only for the ITG part of the total transport, while, as we already remarked, in the pedestal other components are certainly present (apart from ETG modes: subdominant TEMs, MTMs and KBMs).

Particle transport presents partly similar features. The radial particle flux Γ turns out to be generally larger in the outer region of the pedestal ($\rho_t \gtrsim 0.97$) than in the inner part ($\rho_t \lesssim 0.97$), as shown in figure 13. Let us first consider pulse #84793 (left panel) and #91554 (right panel): for the nominal isotope the turbulent fluxes are lower than the neoclassical values in the inner region, and larger in the outer region. The change of the isotope mass results in an increase of Γ if $m_\mathrm{D}\to m_\mathrm{H}$ (pulse #84793), againg localized in the outer domain, making the outward turbulent flux dominate over the neoclassical flux, and in a decrease of Γ if $m_\mathrm{H}\to m_\mathrm{D}$ (pulse #91554), making the turbulent flux largely suppressed and comparable to the neoclassical one. A clear anti-gb-scaling is thus found also for the particle transport, not only for the heat transport.

An anti-gb-scaling occurs also for the high-pressure shot #84796 (figure 13, mid panel), which nevertheless presents quantitatively different transport properties with respect to

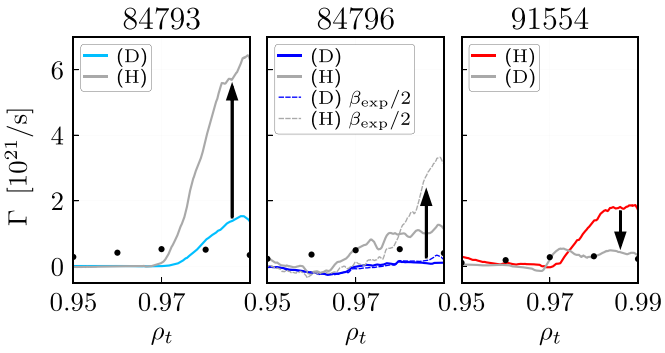


Figure 13. Particle fluxes integrated over the flux surfaces for the nominal (colored lines) and switched (gray lines) isotope from global nonlinear GENE simulations. For pulse #84796 the D/H fluxes are also shown for $\beta = \beta_{\rm exp}/2$ (dashed lines). As a reference, the black dots represent the local neoclassical fluxes of figure 2.

the other two cases. Here the turbulent particle flux is everywhere lower than the neoclassical values for the nominal isotope, and lower than the other two pulses as well, while, as we saw, the heat flux is larger. When $m_{\rm D} \to m_{\rm H}$, Γ becomes larger in the outer region, but still lower than the other pulses.

We have already remarked in section 2 that differences exist between this case and the other two also in the MHD stability context [6], the former (#84796) being close to the ideal PB boundary, and the others (#84793 and #91554) lying on the stable region of the j–α diagram, where other physical mechanisms are likely to play a role in setting the plasma profiles. Particle transport due to ρ_i-scale turbulence—indeed higher for #84793 and #91554 with the nominal isotope—may be among these mechanisms. We note here that one of the main differences between pulse #84796 and the other two pulses is the value of β, important for ITG mode stabilization. For instance, the electron beta at $\rho_t = 0.95$ (pedestal top) is $\beta_e = 1.6 \times 10^{-3}$ for pulse #84793 and #91554, and $\beta_e = 2.5 \times 10^{-3}$ for pulse #84796. As an exercise, assuming the same macroscopic profiles and equilibrium, we artificially reduced the value of β_e for the latter, taking one half of its experimental value (we remark that this modification is unphysical and inconsistent with the equilibrium, the drifts, and the plasma profiles, kept instead unchanged). The result is also shown in figure 13, mid panel. The change of β_e has an impact mainly on the H case, making the Γ profile more similar (peaked outwards) to #84793 in H. The nominal D case is on the other hand practically unchanged with respect to $\beta = \beta_{\rm exp}$, likely due to the dominant effect of the $\omega_{E\times B}$ suppression in the edge.

Further work is certainly needed to understand in more detail the features of ρ_i-scale turbulence. However, based on this study, we might infer a natural tendency of ρ_i-scale turbulence to increase the particle transport for a decreasing isotope mass, and possibly to set the density profile to a lower gradient and consequently to lower pedestal top values. On the other hand, a flattening of the density brings to modified η and $\omega_{E\times B}$ profiles, with implications on the saturated transport levels from ITG turbulence. For a more quantitative evaluation, this study should be reconsidered in flux-driven conditions.

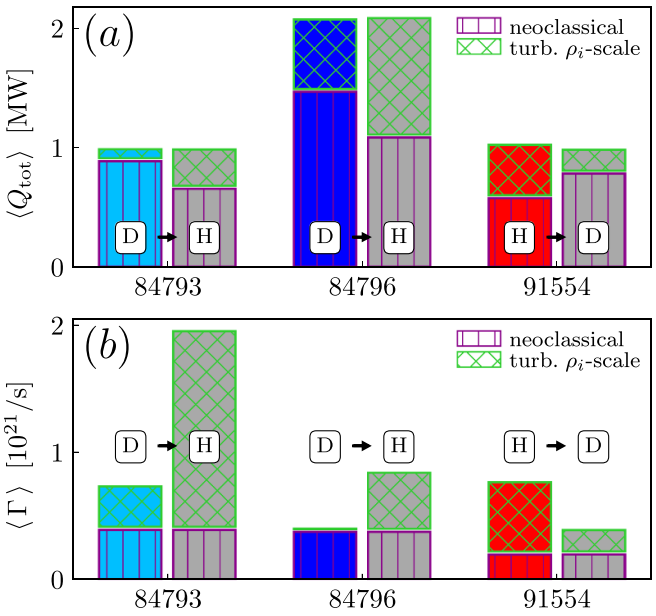


Figure 14. Radially-averaged total heat fluxes $Q_i + Q_e$ (a) and particle fluxes Γ (b) due to neoclassical and ρ_i-scale turbulent transport for the nominal isotope (left, colored bars) and for the switched isotope (right, gray bars).

8. Summary

Three JET-ILW pulses have been considered for a comparative analysis of the pedestal heat and particle transport, two with D as main ion species and one with H, such that a D/H pair has approximately the same input power and the other one the same stored energy. In order to focus on the isotope effect, we have also imposed an artificial change of the main gas isotope, $m_{\rm D} \to m_{\rm H}$ or $m_{\rm H} \to m_{\rm D}$, with the aim to disentangle pure isotope effects from profile effects, introducing an inconsistency between transport and profiles.

The role of neoclassical and turbulent transport has been investigated using the gyrokinetic code GENE with the assumption of scale separation, i.e. treating the ranges $k_y\rho_i \sim 1$ and $k_y\rho_e \sim 1$ separately. Indeed, all the three pedestals are characterized by a mixed ITG/ETG turbulent regime, and by a significant neoclassical heat transport level.

Concerning heat transport, ρ_e-scale (ETG) turbulence has been confirmed to be a relevant vehicle for the electron heat channel, but not for the isotope effect itself. On the other hand, while neoclassical transport provides a gB-scaling of the ion heat transport, ρ_i-scale (mostly ITG) turbulence is characterized by an anti-gB-scaling of the related heat transport, primarily due to the different normalized $\omega_{E\times B}$ shearing rate in species units. A summarizing plot showing the radially-averaged (ion + electron) heat fluxes due to the neoclassical and ρ_i-scale turbulent transport is in figure 14(a). Interestingly, the switch of the ion mass $m_{\rm D} \leftrightarrow m_{\rm H}$ does not generate a net increase or decrease of the total heat flux; rather, the two components roughly compensate each other.

Concerning particle transport, while the neoclassical component is unaffected by the main gas isotope mass, an increase

of ρ_i-scale turbulent transport clearly occurs when $m_D \to m_H$ while, conversely, a decrease takes place when $m_H \to m_D$, as summarized in figure 14(*b*) for the radially-averaged flux. This may provide an efficient mechanism to increase the density gradient in D (and even more in T) with respect to H. ITG turbulence, identified as a key ingredient of low wavenumber turbulence in our three pedestals, may therefore cause stiff density profiles with increasing pedestal top density for increasing isotope mass, in agreement with the JET-ILW experimental results [1, 5]. Self-consistent flux-driven simulations are certainly needed to quantify this effect in more detail.

Following the latter claim, we remark that the analysis carried out in this work can be certainly improved. First, we have assumed fixed plasma profiles and $T_i = T_e$, without a sensitivity study within the experimental error bars: small variations of the profiles usually reflect in relevant changes of the logarithmic gradients, with consequences on the turbulent drives and on the $\omega_{E\times B}$ shear. Another assumption to make the problem tractable is the scale separation in nonlinear simulations, which has already revealed its limitations in several contexts of plasma turbulence. Finally, the impurities have been neglected, but they are definitely central to establish quantitave neoclassical and ρ_i-scale turbulent transport levels.

Acknowledgment

We are grateful to J. Hillesheim and C. Roach for helpful discussions. The numerical simulations have been performed on the Marconi supercomputer at Cineca, Italy.

This work has been carried out within the framework of the EUROfusion Consortium, funded by the European Union via the Euratom Research and Training Programme (Grant Agreement No. 101052200 - EUROfusion). Views and opinions expressed are however those of the author(s) only and do not necessarily reflect those of the European Union or the European Commission. Neither the European Union nor the European Commission can be held responsible for them.

ORCID iDs

I. Predebon https://orcid.org/0000-0002-2100-4698
D.R. Hatch https://orcid.org/0000-0002-1625-4385
L. Frassinetti https://orcid.org/0000-0002-9546-4494
L. Horvath https://orcid.org/0000-0002-5692-6772
S. Saarelma https://orcid.org/0000-0002-6838-2194
B. Chapman-Oplopoiou https://orcid.org/0000-0001-9879-2285
T. Görler https://orcid.org/0000-0002-0851-6699
C.F. Maggi https://orcid.org/0000-0001-7208-2613

References

[1] Maggi C.F. *et al* 2018 *Plasma Phys. Control. Fusion* **60** 014045
[2] Maggi C.F. *et al* 2019 *Nucl. Fusion* **59** 076028
[3] Schneider P.A., Hennequin P., Bonanomi N., Dunne M., Conway G.D. and Plank U. 2021 *Plasma Phys. Control. Fusion* **63** 064006
[4] Weisen H. *et al* 2020 *J. Plasma Phys.* **86** 905860501
[5] Schneider P.A. *et al* 2021 *Nucl. Fusion* **62** 026014
[6] Horvath L. *et al* 2021 *Nucl. Fusion* **61** 046015
[7] Nakata M., Nunami M., Sugama H. and Watanabe T.H. 2017 *Phys. Rev. Lett.* **118** 165002
[8] Belli E.A., Candy J. and Waltz R.E. 2020 *Phys. Rev. Lett.* **125** 015001
[9] Hatch D.R. *et al* 2019 *Nucl. Fusion* **59** 086056
[10] Garcia J., Görler T., Jenko F. and Giruzzi G. 2017 *Nucl. Fusion* **57** 014007
[11] Hatch D.R., Hazeltine R.D., Kotschenreuther M.K. and Mahajan S.M. 2018 *Plasma Phys. Control. Fusion* **60** 084003
[12] Jenko F., Dorland W., Kotschenreuther M. and Rogers B. 2000 *Phys. Plasmas* **7** 1904–10
[13] Görler T., Lapillonne X., Brunner S., Dannert T., Jenko F., Merz F. and Told D. 2011 *J. Comput. Phys.* **230** 7053–71
[14] Maggi C.F. *et al* 2015 *Nucl. Fusion* **55** 113031
[15] Maggi C.F. *et al* 2017 *Nucl. Fusion* **57** 116012
[16] Frassinetti L., Beurskens M.N.A., Scannell R., Osborne T.H., Flanagan J., Kempenaars M., Maslov M., Pasqualotto R. and Walsh M. 2012 *Rev. Sci. Instrum.* **83** 013506
[17] GIT repository The mostly used revision for this work has GIT branch hash b2e4a1c (available at: https://gitlab.mpcdf.mpg.de/GENE/gene)
[18] Maeyama S., Idomura Y., Watanabe T.H., Nakata M., Yagi M., Miyato N., Ishizawa A. and Nunami M. 2015 *Phys. Rev. Lett.* **114** 255002
[19] Pueschel M.J., Hatch D.R., Kotschenreuther M., Ishizawa A. and Merlo G. 2020 *Nucl. Fusion* **60** 124005
[20] Maeyama S., Watanabe T.H., Nakata M., Nunami M., Asahi Y. and Ishizawa A. 2022 *Nat. Commun.* **13** 3166
[21] Huysmans G.T.A., Goedbloed J.P. and Kerner W. 1991 Isoparametric bicubic hermite elements for solution of the grad-shafranov equation *Proc. CP90 Conf. on Comp. Physics (Amsterdam, 1990)* (World Scientific Publishing Co.) p 371
[22] Hager R. and Chang C. 2016 *Phys. Plasmas* **23** 042503
[23] Sauter O., Angioni C. and Lin-Liu Y.R. 1999 *Phys. Plasmas* **6** 2834–9
[24] Luce T.C. 2013 *Plasma Phys. Control. Fusion* **55** 095009
[25] Burrell K.H. 1997 *Phys. Plasmas* **4** 1499–1518
[26] Hahm T.S. 1994 *Phys. Plasmas* **1** 2940–4
[27] McDermott R.M. *et al* 2009 *Phys. Plasmas* **16** 056103
[28] Viezzer E. *et al* 2013 *Nucl. Fusion* **53** 053005
[29] Landreman M. and Ernst D.R. 2012 *Plasma Phys. Control. Fusion* **54** 115006
[30] Helander P. and Sigmar D. 2002 *Collisional Transport in Magnetized Plasmas* (Cambridge: Cambridge University Press)
[31] Callen J.D., Groebner R.J., Osborne T.H., Canik J.M., Owen L.W., Pankin A.Y., Rafiq T., Rognlien T.D. and Stacey W.M. 2010 *Nucl. Fusion* **50** 064004
[32] Viezzer E. *et al* 2017 *Nucl. Fusion* **57** 022020
[33] Belli E.A. and Candy J. 2008 *Plasma Phys. Control. Fusion* **50** 095010
[34] Belli E.A. and Candy J. 2011 *Plasma Phys. Control. Fusion* **54** 015015
[35] Landreman M., Parra F.I., Catto P.J., Ernst D.R. and Pusztai I. 2014 *Plasma Phys. Control. Fusion* **56** 045005
[36] Buller S. and Pusztai I. 2017 *Plasma Phys. Control. Fusion* **59** 105003
[37] Parisi J.F. *et al* 2020 *Nucl. Fusion* **60** 126045
[38] Chapman-Oplopoiou B. *et al* 2022 *Nucl. Fusion* **62** 086028
[39] Parisi J.F. *et al* 2022 *Nucl. Fusion* **62** 086045
[40] Told D., Jenko F., Xanthopoulos P., Horton L.D. and Wolfrum E. 2008 *Phys. Plasmas* **15** 102306
[41] Kotschenreuther M. *et al* 2019 *Nucl. Fusion* **59** 096001
[42] Zhang Y.Z. and Mahajan S.M. 1992 *Phys. Fluids* B **4** 1385–7
[43] Zhang Y.Z. and Mahajan S.M. 1993 *Phys. Fluids* B **5** 2000–20